Nano Research

Open Access

Research Article

Synergizing the activity–stability trade-off in Fe–N–C electrocatalysts towards efficient and durable CO_2-to-CO conversion

Yang Li[1], Yuemei Liu[1], Yang Yuan[2], Xiaojun Lv[3], Junhong Ma[1], Chaoyun Ma[1] ✉, and Hao Jiang[1,4] ✉

[1] *Xinjiang Key Laboratory of Coal Clean Conversion and Chemical Engineering Process, School of Chemical Engineering, Xinjiang University, Urumqi 830046, China*
[2] *Guangyuan China Nuclear Vocational and Technical College, Guangyuan 628003, China*
[3] *State Key Laboratory of Alternate Electrical Power System with Renewable Energy Sources, School of New Energy, North China Electric Power University, Beijing 102206, China*
[4] *Key Laboratory for Ultrafine Materials of Ministry of Education, School of Materials Science and Engineering, East China University of Science and Technology, Shanghai 200237, China*

Cite this article: *Nano Research*, **2026**, *19*, 94908640. https://doi.org/10.26599/NR.2026.94908640

ABSTRACT: Single-atom Fe–N–C electrocatalysts have demonstrated exceptional selectivity toward CO during CO_2 reduction, yet their practical application is severely hindered by the intrinsic activity–stability trade-off. Herein, we report a straightforward *in-situ* sulfidation of Fe-doped zeolitic imidazolate frameworks to construct ZnS nanoparticle-modified S-doped Fe–N–C catalysts (ZnS@Fe–NSC). This approach causes the concurrent formation of $Fe–N_4$ active sites, S doping, and ZnS nanoparticles. *Operando* characterizations and density functional theory (DFT) calculations reveal that ZnS nanoparticles donate electrons to Fe centers with a 0.5 eV negative shift in Fe 2p binding energy and strengthen Fe–N bonds with an increased integrated crystal orbital Hamiltonian population value from −0.94 to −1.30 eV. This electronic modulation accelerates the formation of the key *COOH intermediate and suppresses the hydrogen-induced Fe leaching by over 20-fold. The ZnS@Fe–NSC exhibits a CO Faradaic efficiency of 98.5% at −0.58 V versus reversible hydrogen electrode and maintains over 90% selectivity for 30 h. When integrated into a Zn–CO_2 battery, it delivers a peak power density of 6.2 mW·cm^{-2} and operates stably for 125 h. This work opens an avenue for the rational design of robust single-atom electrocatalysts toward practical CO_2 conversion and beyond.

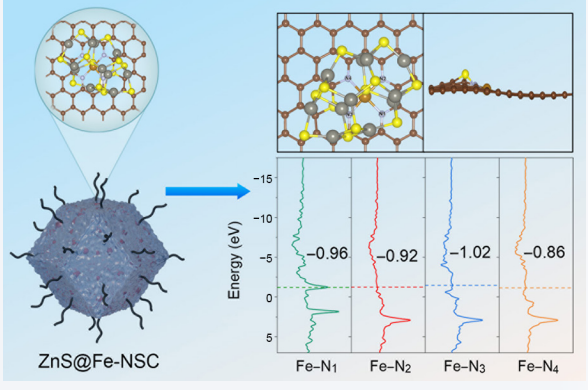

KEYWORDS: electrocatalysts, active sites, CO_2 electroreduction, Zn-based batteries

1 Introduction

Excessive consumption of fossil fuels has caused a sharp increase in atmospheric CO_2 concentrations, triggering a series of severe environmental issues, such as global warming, sea-level rise, and ocean acidification. Efficient utilization of CO_2 resources is a fundamental challenge and of critical importance in addressing climate change [1]. The electrochemical CO_2 reduction reaction (CO_2RR) presents a promising technological approach for converting CO_2 into high-value carbon-based fuels, such as carbon monoxide, ethylene, and ethanol. Among these products, carbon monoxide has attracted significant attention due to its high economic value and wide range of market applications [2–5].

Serving as a crucial bridge between renewable energy and carbon-based chemical synthesis, the techno-economic feasibility of electrocatalytic CO_2RR largely depends on the comprehensive performance of catalysts. Among numerous non-precious metal catalysts, single-atom Fe–N–C materials, featuring atomically dispersed FeN_4 active sites, exhibit high CO selectivity exceeding 90% and low overpotential, positioning them as promising candidates to replace noble metal catalysts, such as Au and Ag [6–9]. Nevertheless, the practical adoption of Fe–N–C materials is fundamentally limited by an inherent trade-off between high activity and long-term operational stability. Under sustained cathodic potentials, the FeN_4 sites are susceptible to structural

Received: January 30, 2026; **Revised:** March 14, 2026
Accepted: March 15, 2026

✉Address correspondence to Chaoyun Ma, mcy_xju_edu@163.com; Hao Jiang, jianghao@ecust.edu.cn

reconstruction, metal leaching, or poisoning by reaction intermediates, resulting in progressive activity decay over the course of tens of hours [10]. This degradation is especially pronounced under acidic or neutral conditions, where proton-assisted dissolution pathways become favorable. This instability primarily arises from the delicate electronic structure of the Fe center. Specifically, a moderate electron deficiency facilitates *COOH formation and CO desorption [11]; however, the same electronic configuration also makes the site susceptible to electrochemical reduction (ECR), over-reduction to metallic Fe, or displacement by adsorbed hydrogen species. Therefore, the primary scientific challenge lies in simultaneously modulating the electronic structure of FeN_4 to enhance its intrinsic activity while strengthening its coordination environment to resist electrochemical degradation. This issue remains inadequately addressed.

Recent advances in heteroatom doping, particularly with sulfur (S), have shown promise in modulating the electronic density of Fe sites, thereby enhancing CO_2 activation and *COOH stabilization [12]. However, such electronic tuning often exacerbates stability issues by increasing surface hydrophilicity and promoting competitive hydrogen adsorption, which accelerates Fe dissolution [13, 14]. Conversely, strategies that incorporate adjacent nanoparticles (NPs, e.g., Fe clusters and ZnS) as electron donors can stabilize FeN_4 sites through charge transfer and strengthened Fe–N bonds [15–21]. Yet, these approaches typically do not address the need for enhanced intrinsic activity. The separation of the two key design principles—namely, activity modulation and stability reinforcement—in most existing methods reflects a fundamental synthetic limitation. This limitation arises from the difficulty in spatially and temporally coordinating multiple functional components within a single catalyst architecture when using conventional multi-precursor methods [11, 22–24].

Herein, we propose a single-precursor *in-situ* sulfidation strategy to concurrently realize the doping of S atom, the confined growth of ZnS nanoparticles, and the anchoring of FeN_4 sites within zeolitic imidazolate framework-8 (ZIF-8)-derived carbon frameworks. The S doping optimizes the adsorption energy barrier of Fe sites towards CO_2 and *COOH intermediates, while ZnS nanoparticles, through electron transfer, lower the Fe oxidation state and enhance Fe–N bond strength, thereby effectively inhibiting H adsorption-induced Fe dissolution. This coupling of molecular scale electronic structure modulation and nanoscale interfacial reinforcement provides a new avenue for addressing the performance bottlenecks of Fe–N–C catalysts. This study will systematically verify the synergistic enhancement effect of this integrated strategy on CO_2RR activity and stability, and elucidate the corresponding structure–performance relationships and reaction mechanisms, laying a theoretical and experimental foundation for the design of practical high-performance CO_2RR electrocatalysts.

2 Results and discussion

2.1 Preparation and characterization of the catalysts

Figure 1(a) illustrates the synthesis schematic of the ZnS nanoparticle-modified S-doped Fe–N–C catalysts (ZnS@Fe–NSC). The strategy encompasses the implementation of *in-situ* sulfur doping, derived from SO_4^{2-} anions, in conjunction with the self-assembly of ZnS, to facilitate the construction of a nanotubular ZnS@Fe–NSC electrocatalyst. This catalyst is synthesized from a ZIF-8 precursor. Specifically, a mixed solution of $Fe_2(SO_4)_3$ and $ZnSO_4{\cdot}7H_2O$ was added to a 2-methylimidazole (2-MeIM) solution to form an Fe-doped ZIF-8 precursor. Subsequently, the precursor was subjected to pyrolysis at a temperature of 900 °C under an N_2 atmosphere for a duration of 2 h. In the course of the pyrolysis process, SO_4^{2-} functions as the sulfur source, thereby facilitating the *in-situ* doping of S into the Fe–N–C matrix. Concurrently, the Zn sites from the ZIF-8 framework react with the S released from the decomposition of SO_4^{2-} to form ZnS nanoparticles. The presence of ZnS has also been demonstrated to facilitate the formation of carbon nanotubes. Concurrently, the decomposition and carbonization of 2-MeIM yield N-doped carbon. In order to facilitate a controlled comparison, S-undoped Fe–NC and ZnS-free Fe–NC samples were prepared in conjunction with the primary materials, employing the same regulated metal salt conditions.

The morphology and microstructure of the ZnS@Fe–NSC catalyst were characterized using scanning electron microscopy (SEM) and high-resolution transmission electron microscopy (HRTEM). The SEM results indicate that the as-prepared ZnS@Fe–NSC sample largely retained the structural morphology of ZIF-8 (Fig. 1(b) and Figs. S1 and S2 in the Electronic Supplementary Material (ESM)). HRTEM image reveals that the catalyst is decorated with a high density of ZnS nanoparticles (Fig. 1(c)). Aberration-corrected high-angle annular dark-field scanning TEM (AC-HAADF-STEM) image of ZnS@Fe–NSC (Fig. 1(d)) reveals the presence of bright, isolated, and densely distributed dots on the carbon matrix, providing direct evidence for the atomic dispersion of iron species. The quantification of the optimal Fe loading was performed using inductively coupled plasma optical emission spectrometry (ICP-OES), which yielded a value of 2.24 wt.% (Table S1 in the ESM). Elemental mapping images (Figs. 1(e) and 1(f)) confirm the homogeneous distribution of C, Fe, N, O, Zn, and S throughout the ZnS@Fe–NSC matrix, validating the effectiveness of the *in-situ* transformation strategy. The X-ray diffraction (XRD) profiles of Fe–N–C and Fe–NSC exhibit only two broad peaks located at approximately 25° and 44°, which are attributed to the (002) and (101) planes of graphitic carbon, respectively. In contrast, the ZnS@Fe–NSC sample exhibited additional distinct diffraction peaks at 28.4°, 30.5°, and 47.5°, corresponding to the characteristic reflections of ZnS, thereby further confirming the successful *in-situ* loading of ZnS (Fig. 1(g)).

The electronic states and coordination environments of the composites were systematically investigated by X-ray photoelectron spectroscopy (XPS). The survey spectra confirm the coexistence of Zn, S, N, Fe, and C (Fig. S3 and Table S2 in the ESM). This finding is highly consistent with the energy dispersive X-ray spectroscopy (EDS) mapping results (Figs. 1(e) and 1(f)). The deconvolution of the Fe 2p spectra indicates the presence of Fe–N coordination along with mixed Fe^{2+} and Fe^{3+} valence states (Fig. 2(a)). It is noteworthy that the Fe species in ZnS@Fe–NSC and Fe–NC manifest more reduced characteristics in comparison to Fe–NSC. This observation is substantiated by a negative shift in the Fe 2p binding energy of approximately 0.5 eV. For ZnS@Fe–NSC, the energy difference was found to be 0.5 eV compared to Fe–NSC. This negative binding energy shift is primarily attributed to the electron-donating nature of ZnS, which enhances the electron density around the Fe centers in ZnS@Fe–NSC through electron transfer. The modulation of the overall electronic structure of the material, particularly the increase in electron density at the Fe centers, is also significantly reflected in the chemical states of its sulfur species.

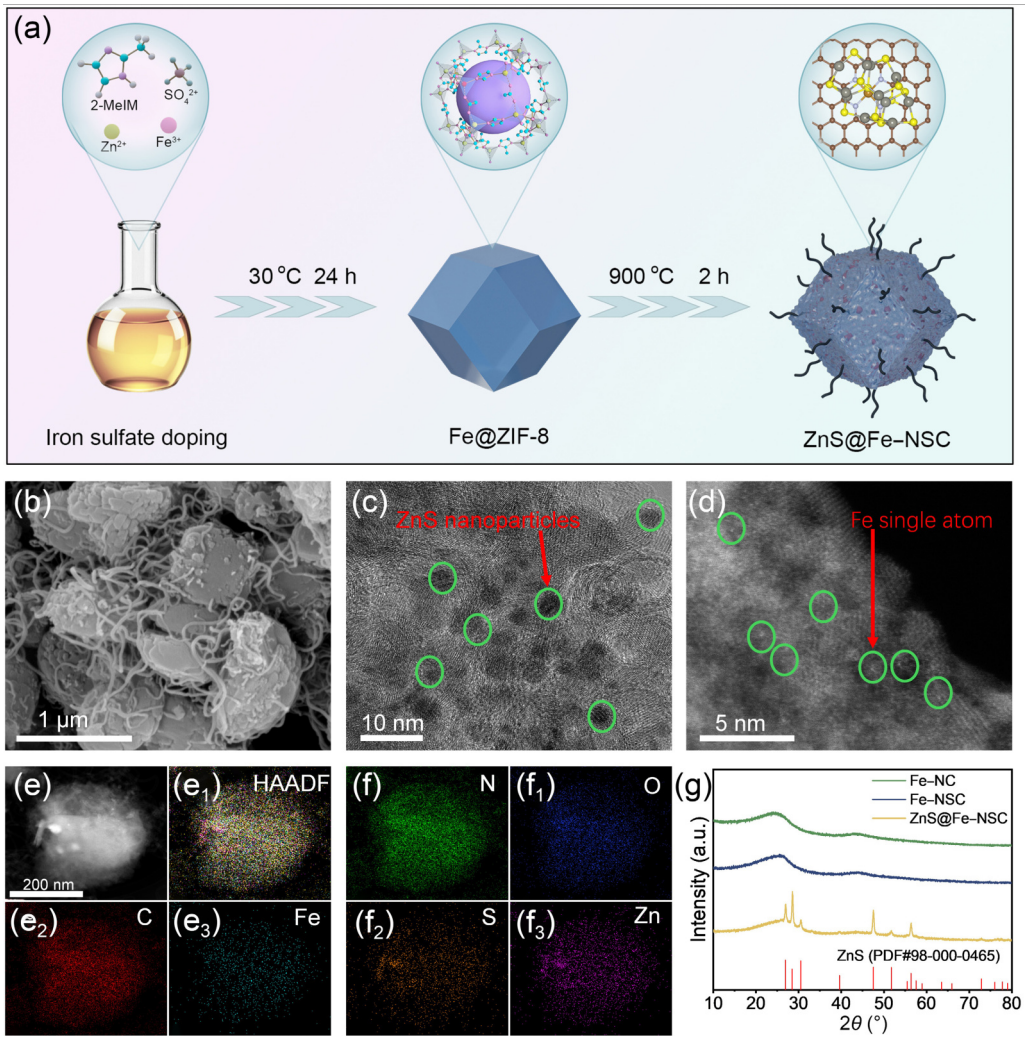

Figure 1 (a) Schematic illustration of the synthesis of ZnS@Fe–NSC. (b) SEM image of ZnS@Fe–NSC. (c) HRTEM image of ZnS@Fe–NSC. (d) AC-HAADF-STEM of ZnS@Fe–NSC. ((e) and (f)) EDS mapping images of ZnS@Fe–NSC. (g) XRD patterns of Fe–NC, Fe–NSC, and ZnS@Fe–NSC.

A comparison of the S 2p spectrum of Fe–NSC with that of ZnS@Fe–NSC reveals significant differences. The characteristic peak at 162.0 eV in the ZnS@Fe–NSC sample corresponds to a Zn–S metal–sulfur bond, whereas no M–S signal peak is observed at 162.0 eV in the Fe–NSC sample, indicating the absence of detectable metal sulfide species. Conversely, the double peak observed at 164.8 eV (S $2p_{3/2}$) and 165.8 eV (S $2p_{1/2}$) is attributed to C–S–C covalent bond structures, while the characteristic peak at 169.2 eV is attributed to C–SO_x–C oxidized sulfur species (Fig. 2(b)). Furthermore, deconvolution analysis of the N 1s spectra (Fig. 2(c)) reveals four characteristic peaks at 398.6, 400.5, 401.3, and 403.0 eV, corresponding to pyridinic nitrogen (pyridinic-N), metal-coordinated nitrogen (Fe–N), pyrrolic nitrogen (pyrrolic-N), and oxidized nitrogen (oxidized-N), respectively. It is noteworthy that pyridinic nitrogen, as the dominant nitrogen species (with the highest proportion), shows a significant increase in content with higher sulfur doping, reaching its maximum value particularly in ZnS@Fe–NSC (Table S3 in the ESM). As stated in the extant literature, pyridinic-N has been demonstrated to effectively promote the adsorption and activation processes of CO_2 molecules by enhancing the Lewis acid-base properties of the material surface [25].

Subsequently, theoretical calculations are conducted to ascertain that ZnS provides electrons to the Fe site. For this purpose, as illustrated in Fig. 2(d), the graphene plane with FeN_4-S/C as the primary structure is employed as the structural model of Fe single-atom catalysts (SACs). Subsequently, ZnS particles were positioned above the graphene plane, adjacent to the FeN_4-S/C position. The charge density difference plot in Fig. 2(e) reveals the transfer of electrons from the particles to the carbon plane, which enriches the electron cloud density position at the Fe site. The calculated results of the Bader charge indicate that the electron transport of ZnS to the Fe site is consistent with the XPS results. A thorough analysis of the S 2p spectra (Fig. 2(b) and Table S4 in the ESM) led to the identification of three distinct states.

Changes in the electronic structure and chemical composition of the material are inevitably accompanied by evolution of its physical structure. Raman spectroscopy analysis (Fig. 2(f)) unequivocally substantiates this assertion by distinctly exhibiting characteristic vibration peaks at 1352 cm^{-1} (D band) and 1580 cm^{-1} (G band) [26, 27]. The intensity ratios (I_D/I_G) were measured as 1.01 for Fe–NC, 1.05 for Fe–NSC, and 1.21 for ZnS@Fe–NSC, respectively. This increasing I_D/I_G trend (ZnS@Fe–NSC > Fe–NSC > Fe–NC) indicates that the dual-doped system (ZnS@Fe–NSC) possesses a higher structural defect density. This phenomenon can be attributed primarily to the greater steric hindrance effect of the

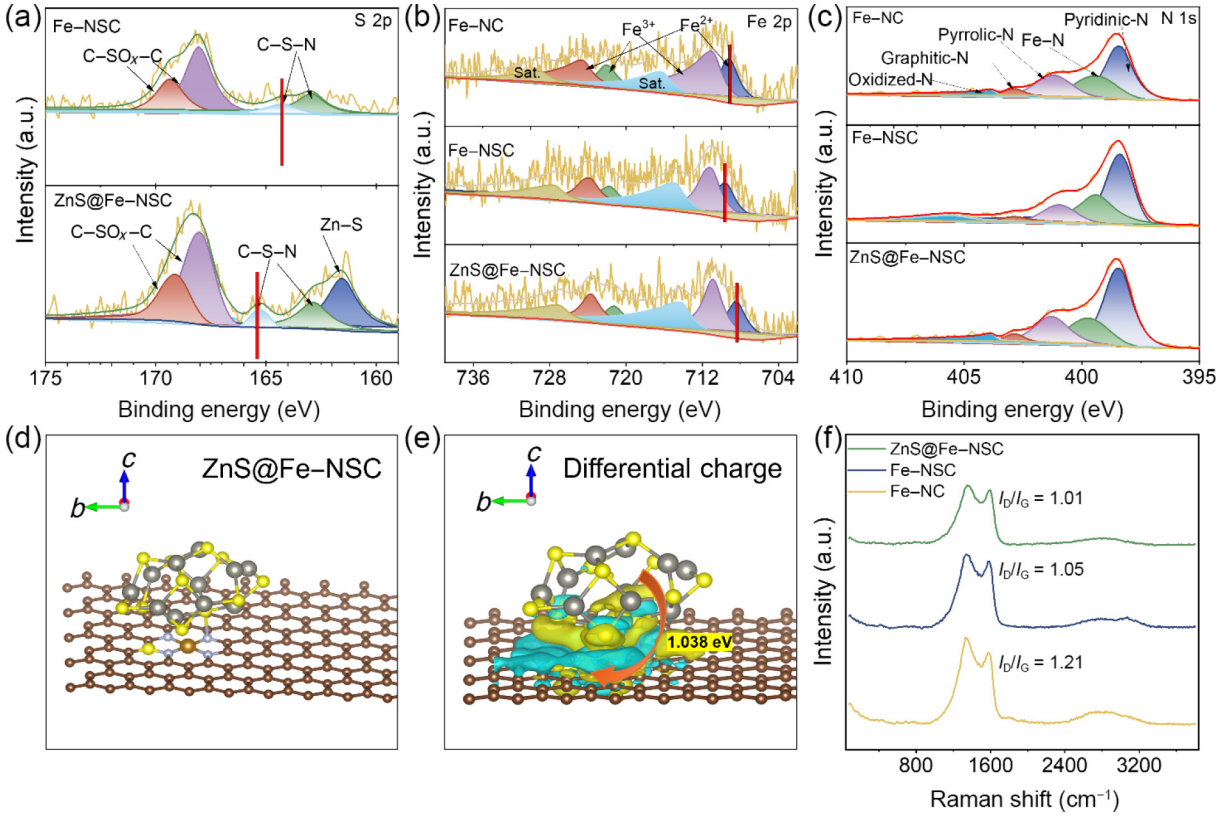

Figure 2 (a) Fe 2p XPS spectra of ZnS@Fe–NSC, Fe–NSC, and Fe–NC. (b) S 2p XPS spectra of ZnS@Fe–NSC and Fe–NSC. (c) N 1s XPS spectra of ZnS@Fe–NSC, Fe–NSC, and Fe–NC. (d) Theoretical model of ZnS@Fe–NSC. (e) Charge density difference of ZnS@Fe–NSC. (f) Raman spectra of ZnS@Fe–NSC, Fe–NSC, and Fe–NC.

sulfur atom (atomic radius 1.04 Å) compared to carbon (0.77 Å) and nitrogen (0.75 Å). The doping process of sulfur readily induces distortion in the hexagonal graphite lattice [28]. Furthermore, the co-doping effect of N/S can synergistically induce the formation of more carbon framework defects [11]. This structural characteristic can facilitate the exposure of catalytically active sites and optimize the mass transfer process.

It is important to note that the *in-situ* sulfidation strategy using SO_4^{2-} as the sulfur source leads to an intrinsically coupled system, where the formation of ZnS nanoparticles and the doping of sulfur into the carbon lattice (C–S–C) occur simultaneously during pyrolysis. This inherent coupling makes it synthetically challenging to obtain a control sample containing ZnS but completely free of S-doping without altering the precursor chemistry. Nevertheless, the distinct chemical states of sulfur observed in the high-resolution S 2p XPS spectra (Fig. 2(b) and Table S4 in the ESM) allow us to differentiate the two species: The peak at 162.0 eV uniquely corresponds to Zn–S bonds in ZnS nanoparticles, while the doublet at 164.8/165.8 eV arises from C–S–C covalent structures. This spectroscopic evidence confirms that ZnS exists as a separate nanophase rather than merely contributing to lattice doping. Therefore, the electronic modulation observed at the Fe centers (the 0.5 eV negative shift in Fe 2p, Fig. 2(a)) can be primarily attributed to interfacial charge transfer from ZnS to Fe–N_4 sites, as further supported by our charge density difference analysis (Fig. 2(e)). The subsequent stability and density functional theory (DFT) results will provide additional evidence to decouple the roles of these two components.

2.2 Electrochemical performance of CO_2 reduction

The CO_2 electroreduction (CO_2RR) performance of the catalysts was systematically evaluated using a three-electrode system with an H-type electrolysis cell. The experiment employed a proton exchange membrane to separate the anode and cathode chambers, with both chambers filled with 25 mL of 0.5 M $KHCO_3$ electrolyte. During the pre-electrolysis stage, N_2/CO_2 gas was introduced for 30 min to thoroughly remove dissolved oxygen, and catalytic activity was verified by linear sweep voltammetry (LSV). The LSV curves in Fig. 3(a) show that the LSV response currents of all catalysts in the CO_2-saturated 0.5 M $KHCO_3$ electrolyte were significantly higher than those in the N_2 environment (Fig. 3(a) and Fig. S4 in the ESM), indicating that Fe–NSC, ZnS@Fe–NSC, and Fe–NC all exhibited CO_2RR activity. Furthermore, compared to the other two catalysts, ZnS@Fe–NSC exhibited the highest current density and a lower onset potential in the CO_2-saturated 0.5 M $KHCO_3$ electrolyte, indicating its optimal CO_2RR activity. The catalytic activity and product selectivity were measured using chronoamperometry. Online gas chromatography detected CO and H_2 as the main gas products, with the total Faradaic efficiency (FE) close to 100%, and liquid-phase nuclear magnetic resonance (NMR) showed no liquid products (Fig. S5 in the ESM). As can be seen from Fig. 3(b), ZnS@Fe–NSC exhibited the highest FE toward CO (FE_{CO}) at all evaluated potentials among all the catalysts. Interestingly, Fe–NSC achieved an FE_{CO} of 94.56% at −0.58 V vs. reversible hydrogen electrode (RHE), which showed little difference from that of ZnS@Fe–NSC at −0.58 V vs. RHE (99.53%) and is much higher than that of Fe–NC (83.37%). To rule out the limited improvement of CO_2RR by ZnS, ZnS@NSC loaded only with ZnS was synthesized, and the CO_2RR performance was tested (Figs. S6 and S7 in the ESM). Furthermore, ZnS@Fe–NSC maintained high CO selectivity and weakly competing hydrogen evolution reaction

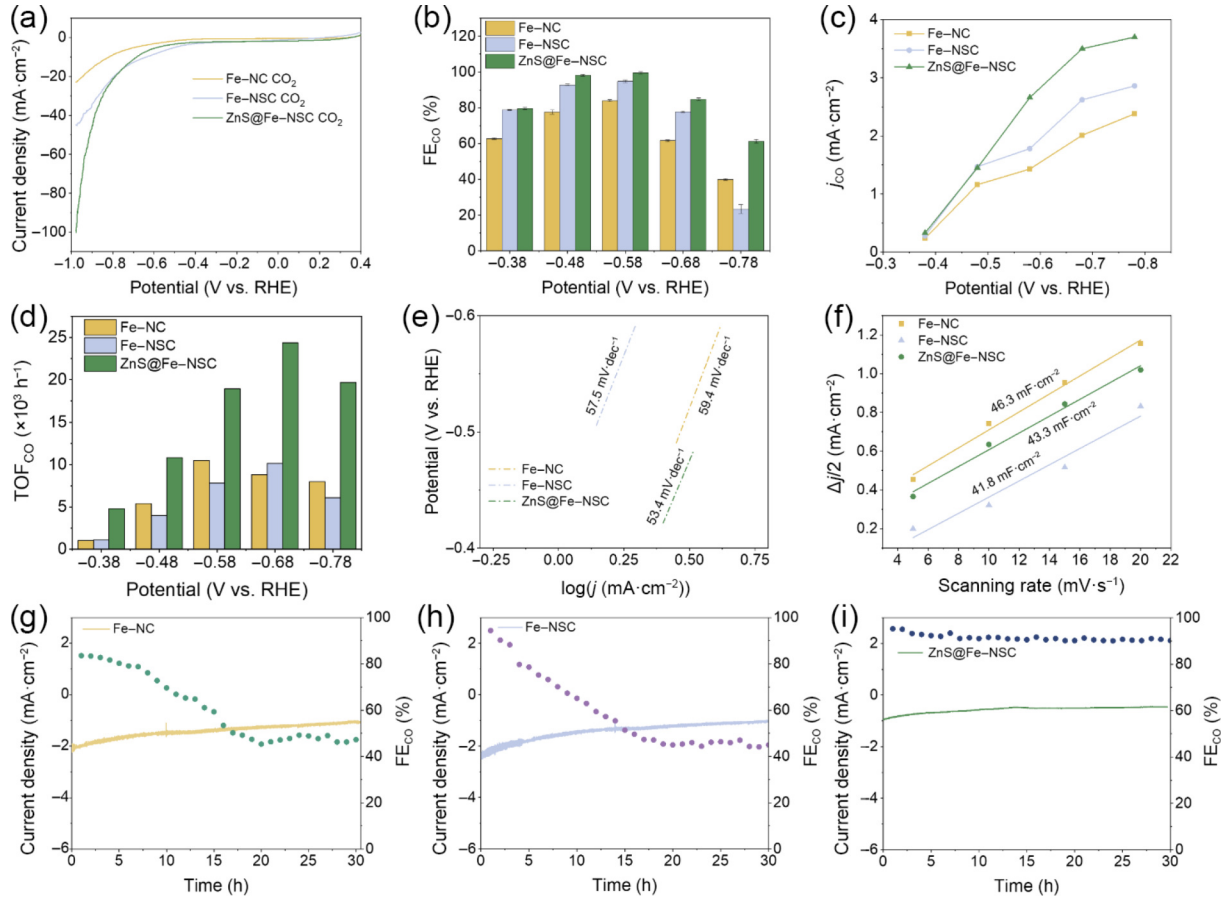

Figure 3 (a) LSV curves of ZnS@Fe–NSC, Fe–NSC, and Fe–NC in CO_2-saturated 0.5 M $KHCO_3$ solution. (b) FE_{CO} of ZnS@Fe–NSC, Fe–NSC, and Fe–NC at different potentials. (c) Carbon monoxide current density (j_{CO}) of ZnS@Fe–NSC, Fe–NSC, and Fe–NC at different potentials. (d) TOF_{CO} of ZnS@Fe–NSC, Fe–NSC, and Fe–NC. (e) Tafel slopes of ZnS@Fe–NSC, Fe–NSC, and Fe–NC. (f) Electrochemical double-layer capacitance measurements of ZnS@Fe–NSC, Fe–NSC, and Fe–NC. ((g)–(i)) Stability test under −0.58 V vs. RHE of Fe–NC, Fe–NSC, and ZnS@Fe–NSC.

(HER) within a broad potential window (−0.4 to −0.8 V) (Fig. 3(b) and Fig. S8 in the ESM). The partial current density for CO indicates that the ZnS@Fe–NSC system exhibits the highest current density across the entire potential range, followed by Fe–NSC and then Fe–NC (Fig. 3(c)). The turnover frequency (TOF) calculated based on Fe active sites further confirms that ZnS@Fe–NSC reaches a TOF toward CO production (TOF_{CO}) of 24,386 h^{-1} at −0.68 V vs. RHE (Fig. 3(d)), which is 1.6 times and 5 times that of Fe–NSC (~ 15,000 h^{-1}) and Fe–NC (< 5000 h^{-1}), respectively, indicating that S doping significantly enhances the intrinsic activity of individual Fe sites. The Tafel slopes for Fe–NC, Fe–NSC, and ZnS@Fe–NSC are 59.4, 57.5, and 53.4 mV·dec^{-1}, respectively (Fig. 3(e)). The decreasing Tafel slope implies significantly accelerated kinetics for CO production, which may be related to enhanced reaction kinetics associated with protonation and subsequent *COOH formation, indicating that S doping and the introduction of ZnS effectively accelerate the formation step of the *COOH intermediate.

To investigate the origin of the high performance of ZnS@Fe–NSC, the electrochemically active surface area (ECSA) was estimated by measuring the double-layer capacitance (C_{dl}), as shown in Fig. 3(f) and Fig. S9 in the ESM. Surprisingly, the ECSA values of Fe–NC (46.37 mF·cm^{-2}), Fe–NSC (43.38 mF·cm^{-2}), and ZnS@Fe–NSC (41.84 mF·cm^{-2}) showed little difference, indicating that the enhancement in CO_2RR activity and selectivity did not depend on the electrochemically active surface area but rather on the improvement in intrinsic activity.

Stability is also one of the important performance metrics of catalysts. The durability of the catalysts was systematically evaluated through chronoamperometric electrolysis at −0.58 V vs. RHE for 30 h (Figs. 3(g)–3(i) and Figs. S10 and S11 in the ESM). The tests revealed that all three catalysts exhibited varying degrees of current density decay. ZnS@Fe–NSC showed the best performance retention with 11.32% decay, while Fe–NSC demonstrated the poorest stability with 56.54% decay (loss of over half its initial activity). Fe–NC showed significant activity degradation with 38.8% decay. Notably, ZnS@Fe–NSC maintained FE_{CO} above 90% throughout the entire testing period, demonstrating exceptional operational stability. In comparison, Fe–NC experienced nearly 30% selectivity decay after 30 h, while Fe–NSC lost over 30% of its selectivity within approximately 10 h (Fig. S12 in the ESM). These results indicate that while S doping enhances CO_2RR activity, it reduces catalyst stability, whereas the introduction of ZnS improves catalyst stability. This performance advantage was further verified by monitoring the Fe element in the electrolyte. ICP-mass spectrometry (MS) analysis (Table S5 in the ESM) showed that after 30 h of electrolysis, only 0.0055 μg·mL^{-1} of Fe leaching was detected for ZnS@Fe–NSC. Compared to the total Fe loading of the catalyst, the loss rate was less than 0.5%, while the values for Fe–NSC and Fe–NC were 10% and 8.1%, respectively (Fig. S13 in the ESM). These results indicate that the single-atom Fe sites in ZnS@Fe–NSC were well preserved, further confirming the stabilizing effect of ZnS on the material structure.

To further verify the structural robustness of the catalyst under operating conditions, post-electrolysis characterizations were conducted on the ZnS@Fe–NSC catalyst after the 30 h stability test. XRD analysis (Fig. S14 in the ESM) revealed that the characteristic peaks corresponding to ZnS (at 28.4°, 30.5°, and 47.5°) remained unchanged in both position and intensity compared to the fresh catalyst, confirming the excellent structural stability of ZnS nanoparticles during long-term CO_2RR. Furthermore, XPS analysis of the used catalyst (Fig. S15 in the ESM) showed that the Fe 2p binding energy and the Fe–N species remained nearly identical to those of the fresh sample, indicating that the atomic dispersion and coordination environment of Fe–N_4 active sites were well preserved. The S 2p spectrum still exhibits the peak at 162.0 eV corresponding to Zn–S bonds, confirming the preservation of ZnS nanoparticles after long-term electrolysis (Fig. S16 in the ESM). The retained ZnS nanoparticles and intact Fe–N_4 sites collectively account for the outstanding durability of ZnS@Fe–NSC, consistent with the negligible Fe leaching (< 0.5%) observed by ICP-MS (Table S5 in the ESM).

2.3 Zn–CO_2 battery (ZCB)

Indeed, owing to the deliberate design of the catalyst, the excellent CO_2RR activity and satisfactory stability endow ZnS@Fe–NSC with potential for practical applications. Based on the bifunctional CO_2 reduction/oxygen evolution reaction (CO_2RR/OER) characteristics of the ZnS@Fe–NSC catalyst, this study constructed a ZCB system using coated carbon paper as the cathode and a zinc plate as the anode (Fig. 4(a)). The discharge principle of this battery involves the dissolution reaction of the polished zinc anode in the anolyte (6 M KOH + 0.2 M Zn $(CH_3COO)_2$), generating Zn_{44} ions and releasing electrons, while simultaneously driving the efficient reduction of CO_2 to CO at the cathode through electron transfer. During the charging process, the reaction path is reversible, with the OER occurring at the cathode and the directional deposition of zinc occurring at the anode. Electrochemical performance tests demonstrated that this battery achieved a peak power density of 6.2 mW·cm^{-2} at a current density of 16 mA·cm^{-2} (Fig. 4(c)), a value significantly superior to those of control catalysts and recently reported similar systems (Table S6 in the ESM). It is noteworthy that zinc anodes are prone to issues, such as corrosion, self-corrosion, and dendrite growth, in high-concentration KOH electrolyte, which seriously affect the cycling stability of the battery. To address this, this study employed a 6 M KOH electrolyte system, extensively validated in literature, to balance anode stability and battery performance [23, 29]. The open-circuit voltage (OCV) of the battery remained stable at approximately 2.0 V, closely matching the multimeter measurement results (Fig. 4(b)). Further analysis of discharge curves at different current densities (Fig. 4(d)) revealed that the ZnS@Fe–NSC cathode demonstrated excellent catalytic activity and stability in terms of CO Faradaic efficiency and product selectivity. Through systematic cycling performance tests (Fig. 4(e)), the ZnS@Fe–NSC cathode exhibited long-term cycling stability of 125 h under constant-current discharge at 0.5 mA·cm^{-2}. The discharge voltage remained stable at 1.50 V during individual charge–discharge cycles, and the charge–discharge voltage gap showed no significant change after 125 h of cycling, highlighting its potential for engineering applications as a ZCB cathode material. Notably, the ZCB assembled with this cathode successfully powered a yellow light-emitting diode (LED) (Fig. 4(f)), verifying its practical energy output capability. Through systematic electrochemical characterization and device validation, this study conclusively demonstrated that the ZnS@Fe–NSC catalyst exhibits efficient energy conversion and stable output performance within the reversible ZCB system.

2.4 Mechanism exploration

To further investigate the ECR reaction mechanism on ZnS@Fe–NSC and elucidate the role of S doping at Fe–N_4 sites in

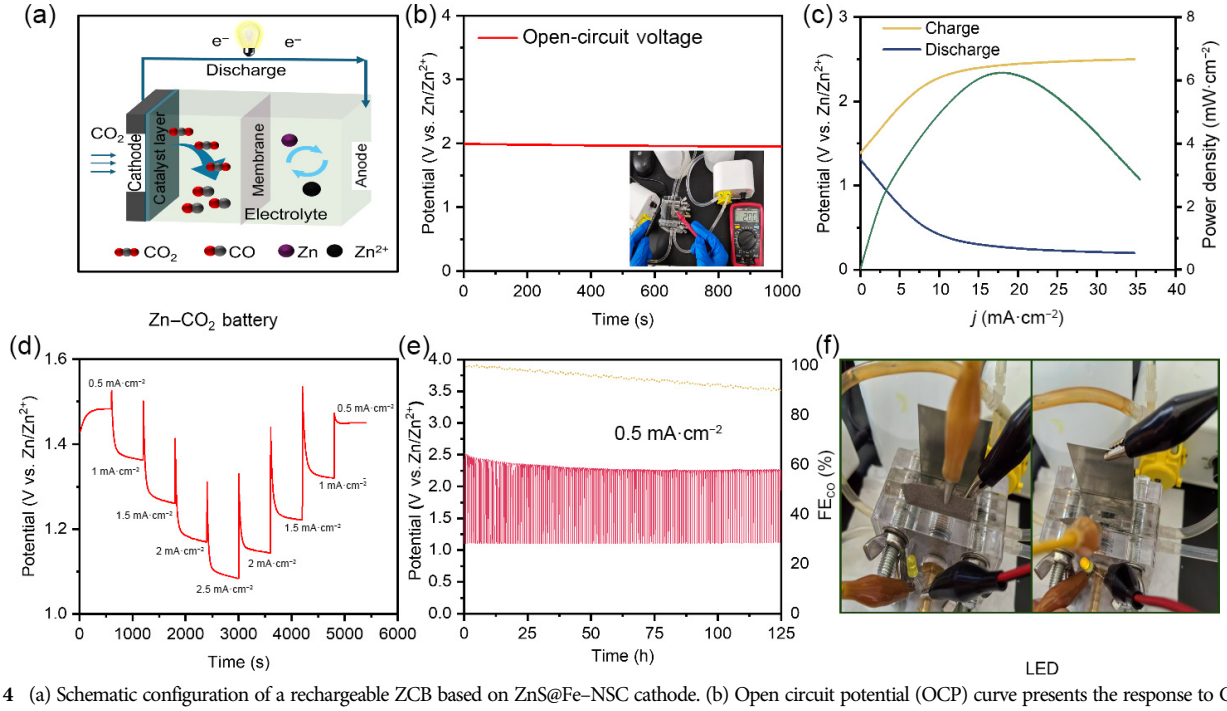

Figure 4 (a) Schematic configuration of a rechargeable ZCB based on ZnS@Fe–NSC cathode. (b) Open circuit potential (OCP) curve presents the response to CO_2. (c) Discharge/charge polarization and power density curves of the ZnS@Fe–NSC cathode-based ZCB (polarization scan rate: 5 mV·s^{-1}). (d) Constant current discharge curves at different current densities. (e) Galvanostatic discharge–charge cycling curves at the current density of 0.5 mA·cm^{-2}. (f) Digital photograph of an LED illuminated by Zn–CO_2 battery.

enhancing CO_2 reduction efficiency, *in-situ* characterization of adsorbed species on the catalyst surface was conducted using attenuated total reflectance Fourier transform infrared (ATR-FTIR) spectroscopy. Figures 5(a)–5(c) show the *in-situ* ATR-FTIR spectra of Fe–NC, Fe–NSC, and ZnS@Fe–NSC, measured in a CO_2-saturated 0.5 M $KHCO_3$ solution over a potential range of −0.1 to −0.9 V vs. RHE. A positive peak observed at 1410 cm^{-1} in all spectra is attributed to the *COOH intermediate, indicating that *COOH formation is the rate-determining step in the ECR process [30, 31]. Furthermore, for ZnS@Fe–NSC and Fe–NSC, the positive H_2O signal at 1635 cm^{-1} gradually weakens with increasing potential, transitions to negative values after −0.5 V, and continues to diminish in intensity. This indicates rapid consumption of H_2O on the surface of ZnS@Fe–NSC and Fe–NSC. In contrast, for Fe–NC, the H_2O signal shows a much weaker attenuation trend. Even beyond −0.8 V, only faint negative features are observed on the Fe–NC catalyst, indicating persistent accumulation of H_2O on the Fe–NC surface. In combination with LSV curves measured in N_2-saturated electrolyte, Fe–NSC and ZnS@Fe–NSC exhibit higher hydrogen evolution activity compared to Fe–NC. The hydrophilicity of the catalysts was further characterized through contact angle measurements. As shown in Fig. S17 in the ESM, S doping enhances the hydrophilicity of both ZnS@Fe–NSC and Fe–NSC, which promotes water adsorption and thereby enhances the water activation capability of these catalysts. It can therefore be inferred that S doping in ZnS@Fe–NSC and Fe–NSC facilitates the dissociation of $*H_2O$ into protons on the catalyst surface, which are subsequently captured by $Fe–N_4$ sites to form *COOH [30, 32, 33]. These results are also consistent with the significant ECR performance of ZnS@Fe–NSC and Fe–NSC.

Subsequently, we investigated the coverage of adsorbed hydrogen (*H) on the catalyst surfaces through electrochemical impedance spectroscopy (EIS) measurements (Fig. 5(e)) and employed a dual-parallel equivalent circuit model to simulate the Nyquist plots (Fig. 5(d) and Figs. S18 and S19 in the ESM). In the EIS analysis, a double parallel equivalent circuit model was used to fit the experimental data (see Fig. 5(d) and Table S7 in the ESM). This model consists of two sets of parallel components connected in series: The first set includes the charge transfer resistance (R_1) and the constant phase angle element (CPE_1), which describe the charge transfer process at the catalyst/electrolyte interface, where R_1 reflects the charge transfer kinetics of the HER, and CPE_1 is related to the

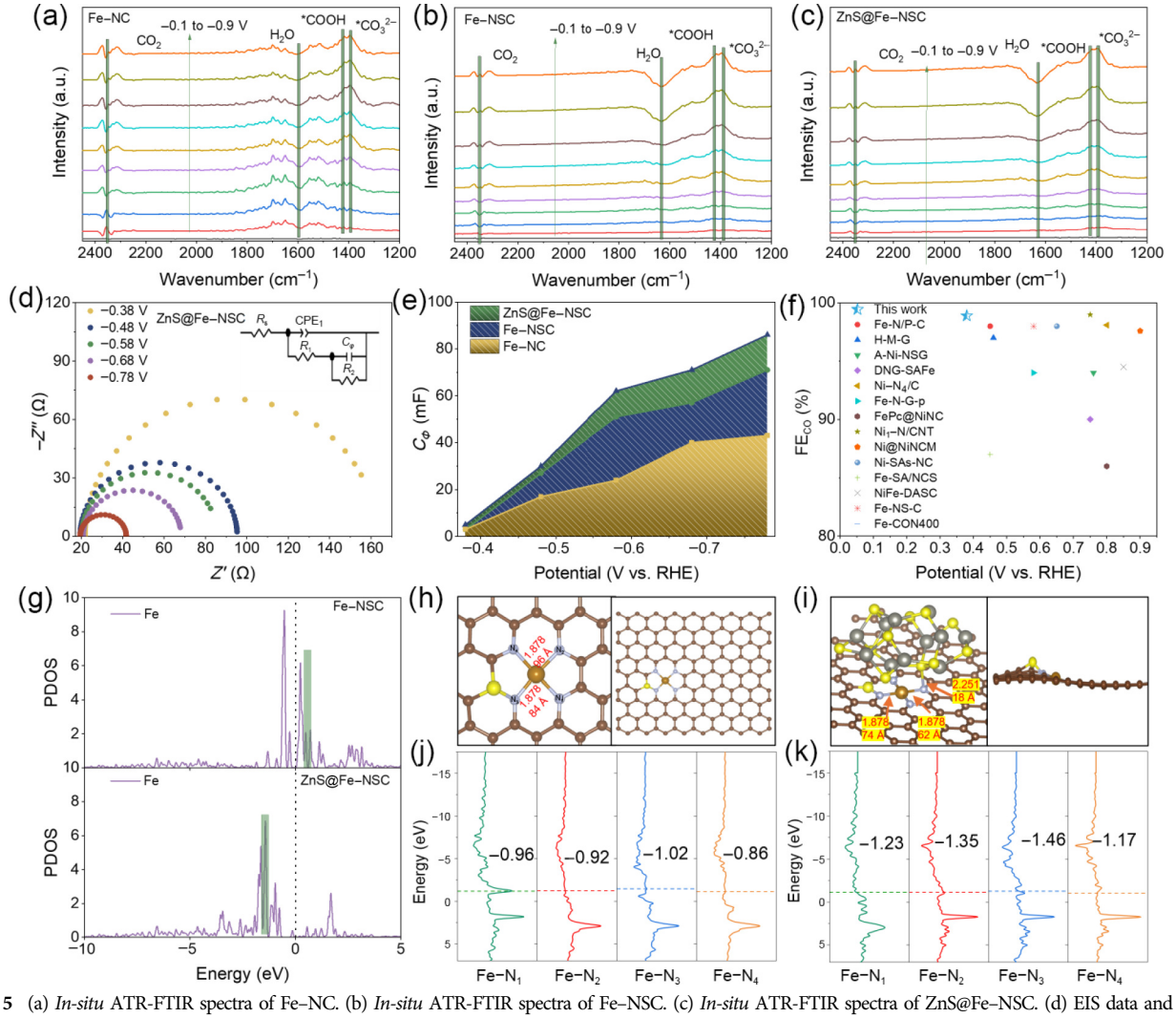

Figure 5 (a) *In-situ* ATR-FTIR spectra of Fe–NC. (b) *In-situ* ATR-FTIR spectra of Fe–NSC. (c) *In-situ* ATR-FTIR spectra of ZnS@Fe–NSC. (d) EIS data and fitting results of ZnS@Fe–NSC. (e) Calculated C_Φ of ZnS@Fe–NSC, Fe–NSC, and Fe–NC at different potentials. (f) FE_{CO} comparison of ZnS@Fe–NSC and typical reference catalysts. (g) The calculated density of states for a Fe 3d orbital of Fe–NSC and ZnS@Fe–NSC. ((h) and (i)) Theoretically computed model of FeN_4-S/C and FeN_4-S/C@ZnS. (j) COHPs of the Fe–N bond in Fe–NSC. (k) COHPs of the Fe–N bond in ZnS@Fe–NSC.

double-layer capacitance; the second set includes the hydrogen adsorption resistance R_2 and the hydrogen adsorption pseudocapacitance (C_Φ), corresponding to the adsorption behavior of hydrogen intermediates (H*) on the catalyst surface, where R_2 characterizes the resistance of the adsorption step, and C_Φ is related to the amount of adsorbed hydrogen. By fitting this circuit model, the contributions of charge transfer and hydrogen adsorption to the HER kinetics can be quantitatively distinguished, and the amount of hydrogen adsorption charge can be calculated based on the variation of C_Φ with the overpotential, thereby providing electrochemical evidence for the existence of the hydrogen spillover effect. As shown in Table S7 in the ESM, ZnS@Fe–NSC and Fe–NSC exhibited higher *H coverage relative to Fe–NC, as quantified by C_Φ. At −0.68 V vs. RHE, the H* coverage of ZnS@Fe–NSC was 2.08 times that of Fe–NC, while Fe–NSC showed 1.92 times the coverage of Fe–NC. These results clearly demonstrate that sulfur doping promotes proton transfer from H_2O. The higher C_Φ value observed for ZnS@Fe–NSC compared to Fe–NSC may be attributed to the introduction of NPs in the Fe–N–C catalyst architecture, which can further accelerate proton transfer by facilitating water dissociation [34, 35]. Therefore, the introduction of ZnS nanoparticles further optimizes the electronic structure of FeN_4 sites through electronic modulation, ensuring sufficient *H supply for the formation of the *COOH intermediate. It is impressive that ZnS@Fe–NSC outperforms most reported M–N–C SAC catalysts for CO_2RR in simultaneously achieving high FE_{CO} and TOF values (Fig. 5(f) and Table S8 in the ESM) [1, 33, 36–38]. This makes ZnS@Fe–NSC a promising catalyst for CO production.

To further investigate the kinetics and stability mechanism, DFT calculations were employed. Figures 5(h) and 5(i) show the optimized geometric structures of FeN_4-S/C and FeN_4-S/C@ZnS, with critical bond lengths labeled. The observation that ZnS effectively transfers electrons to the Fe sites significantly shortens the Fe–N bond length, which is consistent with the enhanced stability of the catalyst. Complementing this, Fig. 2(e) provides the quantitative charge density difference and Bader charge analysis, confirming electron donation from ZnS to the Fe center. The d-band center was studied by examining the projected density of states (PDOS) of the Fe 3d orbitals in the models. It was found that the d-band center of the Fe atom on ZnS@Fe–NSC (−1.42 eV) exhibited a negative shift (ϵ) compared to that on Fe–NSC (0.48 eV) (Fig. 5(g) and Figs. S20 and S21 in the ESM). This indicates a weaker binding interaction between the Fe atom in Fe–NSC and the *COOH/CO intermediates [39]. Furthermore, this negative shift ϵ also enhances the Lewis basicity of the Fe atomic center, promoting the capture of CO_2 and electron transfer [23]. It is noteworthy that the antibonding orbital distribution of FeN_4-S/C@ZnS is narrower than that of FeN_4-S/C, indicating a stronger Fe–N bonding. This results in Fe species being less prone to leaching, a theoretical finding that aligns with the enhanced stability observed experimentally.

Starting from the leaching mechanism of Fe atoms, we aimed to uncover the determining factors influencing the stability of SACs. This was first investigated by calculating the crystal orbital Hamiltonian population (COHP) between the Fe atom and its coordinating N atoms [40, 41] to evaluate the binding strength of the Fe atom on the substrate, and by analyzing changes in the integrated COHP (ICOHP) to examine differences in the metal leaching capability among Fe atoms. Generally, the more negative the ICOHP value and the larger its absolute value, the higher the leaching energy and the more stable the catalyst. As observed in Figs. 5(j) and 5(k), to quantitatively evaluate the local bonding strength, we calculated the COHP for each of the four Fe–N bonds (labeled as Fe–N_4 to Fe–N_4, which correspond to the four distinct nitrogen atoms coordinated to the central Fe atom in the structural models shown in Figs. 5(h) and 5(i)). The COHP peaks near the Fermi level for all four bonds (Fe–N_4 to Fe–N_4) in ZnS@Fe–NSC are enhanced compared to those in Fe–NSC. The corresponding ICOHP values, while those for Fe–NSC are −0.96, −0.92, −1.02, and −0.86 eV. The more negative ICOHP values (i.e., larger in magnitude) of ZnS@Fe–NSC indicate stronger Fe–N bonds, greater resistance to Fe atom leaching, and enhanced catalyst stability.

3 Conclusions

This study introduces an innovative method that employs a single sulfate precursor to simultaneously supply Fe, enable S doping, and synthesize ZnS, thereby effectively mitigating the structural uncertainties commonly associated with conventional multi-precursor approaches. The resulting high-performance ZnS@Fe–NSC catalyst exhibits synergistic enhancement of both catalytic activity and stability for CO_2RR. ZnS@Fe–NSC achieves outstanding CO selectivity (FE_{CO} = 99.53%) and maintains stable operation for over 30 h at a low overpotential of −0.58 V vs. RHE. Furthermore, the assembled Zn–CO_2 battery delivers a peak power density of 6.2 mW·cm^{-2} while operating stably for 125 h, successfully powering an LED device and outperforming most reported Fe-based single-atom catalysts. *In-situ* ATR-FTIR measurements combined with DFT calculations reveal that S doping promotes the dissociation of H_2O into *H on the catalyst surface, which is subsequently captured by Fe–N_4 sites to form *COOH, thereby enhancing FECO. Notably, ZnS nanoparticles enhance the electron density at FeN_4 sites through electron transfer, leading to a 0.5 eV negative shift in the Fe 2p binding energy. This shift concurrently lowers the oxidation state of Fe and strengthens Fe–N bonding, as indicated by a decrease in ICOHP from −0.94 to −1.30 eV, ultimately improving catalyst stability. This work provides a novel strategy for designing highly active and stable M–N–C catalysts and establishes a solid foundation for the practical application of single-atom catalysts in energy conversion devices.

Electronic Supplementary Material: Supplementary material (details of electrochemical testing and fitting and material synthesis) is available in the online version of this article at https://doi.org/10.26599/NR.2026.94908640.

Data availability

All data needed to support the conclusions in the paper are presented in the manuscript and the Electronic Supplementary Material. Additional data related to this paper may be requested from the corresponding author upon request.

Acknowledgements

This work was supported by the National Natural Science Foundation of China (No. 22508331), the "Tianchi Talent" Introduction Program of Xinjiang Uygur Autonomous Region, the Basic Scientific Research Business Expenses of Colleges and

Universities in the Autonomous Region (No. 610225051), and the Major science and technology projects of Xinjiang Uygur Autonomous Region (No. 2024A01001).

Declaration of competing interest

All the contributing authors report no conflict of interests in this work.

Author contribution statement

Y. L.: Data curation, project administration, validation, writing manuscript, experimental design. Y. M. L.: Data curation, project administration, validation, experimental design. Y. Y.: Project administration, data collection. X. J. L. and J. H. M.: Project administration, funding acquisition. C. Y. M. and H. J.: Project administration, funding acquisition, writing manuscript. All the authors have approved the final manuscript.

Use of AI statement

None.

References

[1] Gu, J.; Hsu, C. S.; Bai, L. C.; Chen, H. M.; Hu, X. L. Atomically dispersed Fe^{3+} sites catalyze efficient CO_2 electroreduction to CO. *Science* **2019**, *364*, 1091–1094.

[2] Wang, H. B.; Zhang, H.; Huang, Y.; Wang, H. Y.; Ozden, A.; Yao, K. L.; Li, H. M.; Guo, Q. Y.; Liu, Y. C.; Vomiero, A. et al. Strain in copper/ceria heterostructure promotes electrosynthesis of multicarbon products. *ACS Nano* **2023**, *17*, 346–354.

[3] Gao, D. F.; Arán-Ais, R. M.; Jeon, H. S.; Roldan Cuenya, B. Rational catalyst and electrolyte design for CO_2 electroreduction towards multicarbon products. *Nat. Catal.* **2019**, *2*, 198–210.

[4] Nielsen, D. U.; Hu, X. M.; Daasbjerg, K.; Skrydstrup, T. Chemically and electrochemically catalysed conversion of CO_2 to CO with follow-up utilization to value-added chemicals. *Nat. Catal.* **2018**, *1*, 244–254.

[5] Rommens, K. T.; Saeys, M. Molecular views on Fischer–Tropsch synthesis. *Chem. Rev.* **2023**, *123*, 5798–5858.

[6] Cao, S. F.; Zhou, S. N.; Chen, H. Y.; Wei, S. X.; Liu, S. Y.; Lin, X. J.; Chen, X. D.; Wang, Z. J.; Guo, W. Y.; Lu, X. Q. How can the dual-atom catalyst FeCo–NC surpass single-atom catalysts Fe–NC/Co–NC in CO_2RR?—CO intermediate assisted promotion via a synergistic effect. *Energy Environ. Mater.* **2023**, *6*, e12287.

[7] Liang, S. Y.; Huang, L.; Gao, Y. S.; Wang, Q.; Liu, B. Electrochemical reduction of CO_2 to CO over transition metal/N-doped carbon catalysts: The active sites and reaction mechanism. *Adv. Sci.* **2021**, *8*, 2102886.

[8] Sun, D.; Zhou, J. B.; Rao, D. W.; Zhu, L. Q.; Niu, S. W.; Cai, J. Y.; Fang, Y. Y.; Liu, Y.; Liu, X. M.; Zang, Y. P. et al. Regulating the electron filling state of d orbitals in Ta-based compounds for tunable lithium–sulfur chemistry. *Sustain. Mater. Technol.* **2021**, *28*, e00271.

[9] Huan, T. N.; Ranjbar, N.; Rousse, G.; Sougrati, M.; Zitolo, A.; Mougel, V.; Jaouen, F.; Fontecave, M. Electrochemical reduction of CO_2 catalyzed by Fe–N–C materials: A structure–selectivity study. *ACS Catal.* **2017**, *7*, 1520–1525.

[10] Wu, G.; Zelenay, P. Activity versus stability of atomically dispersed transition-metal electrocatalysts. *Nat. Rev. Mater.* **2024**, *9*, 643–656.

[11] Pan, F. P.; Li, B. Y.; Sarnello, E.; Hwang, S.; Gang, Y.; Feng, X. H.; Xiang, X. M.; Adli, N. M.; Li, T.; Su, D. et al. Boosting CO_2 reduction on Fe–N–C with sulfur incorporation: Synergistic electronic and structural engineering. *Nano Energy* **2020**, *68*, 104384.

[12] Jia, C.; Tan, X.; Zhao, Y.; Ren, W. H.; Li, Y. B.; Su, Z.; Smith, S. C.; Zhao, C. Sulfur-dopant-promoted electroreduction of CO_2 over coordinatively unsaturated Ni–N_2 moieties. *Angew. Chem.* **2021**, *133*, 23530–23536.

[13] Cui, Y.; Ren, C. J.; Wu, M. L.; Chen, Y.; Li, Q.; Ling, C. Y.; Wang, J. L. Structure–stability relation of single-atom catalysts under operating conditions of CO_2 reduction. *J. Am. Chem. Soc.* **2024**, *146*, 29169–29176.

[14] Wang, R. G.; Guo, J. X.; Li, J. S.; Wang, Q. L.; Lv, Z.; Gong, C. R.; Pan, C. F.; Ling, T. Transforming single-atom site to dual-atom site in Fe–N–C catalysts: A universal strategy for enhancing durability in proton-exchange membrane fuel cells. *Angew. Chem., Int. Ed.* **2025**, *64*, e202510671.

[15] Wan, X.; Liu, Q. T.; Liu, J. Y.; Liu, S. Y.; Liu, X. F.; Zheng, L. R.; Shang, J. X.; Yu, R. H.; Shui, J. L. Iron atom-cluster interactions increase activity and improve durability in Fe–N–C fuel cells. *Nat. Commun.* **2022**, *13*, 2963.

[16] Ibraheem, S.; Chen, S. G.; Peng, L. L.; Li, J.; Li, L.; Liao, Q.; Shao, M. H.; Wei, Z. D. Strongly coupled iron selenides-nitrogen-bond as an electronic transport bridge for enhanced synergistic oxygen electrocatalysis in rechargeable zinc–O_2 batteries. *Appl. Catal. B: Environ.* **2020**, *265*, 118569.

[17] Deng, S. L.; Li, C. G.; Feng, W. H.; Cao, Y. W.; Tian, X. C.; Bi, H. T.; Zhou, S.; Wong, C. P.; Dong, Y. F. Ultra-small ZnS enhanced by Fe–N–C for advanced potassium-ion hybrid capacitors: Electronic transfer dynamics and ion adsorption capability. *Nano Energy* **2023**, *106*, 108065.

[18] Wang, P.; Zhao, S. J.; Liu, Z. J.; Han, C. Y.; Wang, S.; Li, J. P. The modulation of catalytic active site and support to construct high-efficiency ZnS/NC–X electrocatalyst for nitrogen reduction. *Nano Res.* **2022**, *15*, 7903–7909.

[19] Gao, X. B.; Wang, Y. C.; Xu, W. C.; Huang, H.; Zhao, K. M.; Ye, H.; Zhou, Z. Y.; Zheng, N. F.; Sun, S. G. Mechanism of particle-mediated inhibition of demetalation for single-atom catalytic sites in acidic electrochemical environments. *J. Am. Chem. Soc.* **2023**, *145*, 15528–15537.

[20] Song, Y. P.; Wang, Y.; Shao, J. Q.; Ye, K.; Wang, Q.; Wang, G. X. Boosting CO_2 electroreduction via construction of a stable ZnS/ZnO interface. *ACS Appl. Mater. Interfaces* **2022**, *14*, 20368–20374.

[21] Liu, Y. M.; Ma, J. H.; Meng, Z. Y.; Ma, C. Y.; Xu, R. Dual-regulated cascade catalysis via spatial synergy and electronic coupling for efficient oxygen reduction reaction. *J. Colloid Interface Sci.* **2025**, *699*, 138212.

[22] Yang, X.; Cheng, J.; Lv, H. K.; Yang, X.; Ding, L. W.; Xu, Y.; Zhang, K.; Sun, W. F.; Zhou, J. H. Sulfur-doped unsaturated Ni–N_3 coordination for efficient electroreduction of CO_2. *Chem. Eng. J.* **2022**, *450*, 137950.

[23] Han, J. W.; Xu, Q.; Rong, J. X.; Zhao, X.; She, P.; Qin, J. S.; Rao, H. Molecular engineering of porous Fe–N–C catalyst with sulfur incorporation for boosting CO_2 reduction and Zn–CO_2 battery. *Adv. Sci.* **2024**, *11*, 2407063.

[24] Huang, K.; Li, R.; Qi, H. D.; Yang, S.; An, S. H.; Lian, C.; Xu, Q.; Liu, H. L.; Hu, J. Regulating adsorption of intermediates via the sulfur modulating dual-atomic sites for boosting CO_2RR. *ACS Catal.* **2024**, *14*, 8889–8898.

[25] Thubsuang, U.; Manmuanpom, N.; Chokaksornsan, N.; Sommut, C.; Singhawat, K.; Payaka, A.; Wongkasemjit, S.; Chaisuwan, T. Efficient CO_2 adsorption on porous carbon with nitrogen functionalities based on polybenzoxazine: High-pressure adsorption characteristics. *Appl. Surface Sci.* **2023**, *607*, 155120.

[26] Choi, K. M.; Jeong, H. M.; Park, J. H.; Zhang, Y. B.; Kang, J. K.; Yaghi, O. M. Supercapacitors of nanocrystalline metal–organic frameworks. *ACS Nano* **2014**, *8*, 7451–7457.

[27] Ferrari, A. C.; Basko, D. M. Raman spectroscopy as a versatile tool for studying the properties of graphene. *Nat. Nanotechnol.* **2013**, *8*, 235–246.

[28] Ito, Y.; Cong, W. T.; Fujita, T.; Tang, Z.; Chen, M. W. High catalytic

activity of nitrogen and sulfur co-doped nanoporous graphene in the hydrogen evolution reaction. *Angew. Chem., Int. Ed.* **2015**, *54*, 2131–2136.

[29] Sun, X. Y.; Yang, S. X.; Mu, X. W.; Li, W.; Sheng, C. C.; Chen, A. Y.; Wen, Z.; Wang, Y. G.; Zhou, H. S.; He, P. A rechargeable "Rocking Chair" type Zn–CO_2 battery. *Angew. Chem., Int. Ed.* **2024**, *63*, e202409977.

[30] Hu, X. Z.; Liu, Y. N.; Cui, W. J.; Yang, X. X.; Li, J. T.; Zheng, S. X.; Yang, B.; Li, Z. J.; Sang, X. H.; Li, Y. Y. et al. Boosting industrial-level CO_2 electroreduction of N-doped carbon nanofibers with confined tin–nitrogen active sites via accelerating proton transport kinetics. *Adv. Funct. Mater.* **2023**, *33*, 2208781.

[31] Wang, X. Y.; Wang, C.; Ren, H. A.; Lu, J. X.; Chen, B. R.; Liu, Y. P.; Guan, Q. X.; Li, W. Accelerating proton and electron transfer enables highly active Fe–N–C catalyst for electrochemical CO_2 reduction. *Adv. Funct. Mater.* **2024**, *34*, 2311818.

[32] Chen, S. Y.; Li, X. Q.; Kao, C. W.; Luo, T.; Chen, K. J.; Fu, J. W.; Ma, C.; Li, H. M.; Li, M.; Chan, T. S. et al. Unveiling the proton-feeding effect in sulfur-doped Fe–N–C single-atom catalyst for enhanced CO_2 electroreduction. *Angew. Chem., Int. Ed.* **2022**, *61*, e202206233.

[33] Liu, C. H.; Wu, Y.; Sun, K. A.; Fang, J. J.; Huang, A. J.; Pan, Y.; Cheong, W. C.; Zhuang, Z. W.; Zhuang, Z. B.; Yuan, Q. H. et al. Constructing FeN_4/graphitic nitrogen atomic interface for high-efficiency electrochemical CO_2 reduction over a broad potential window. *Chem* **2021**, *7*, 1297–1307.

[34] Chen, D. T.; Zhang, L. H.; Du, J.; Wang, H. H.; Guo, J. Y.; Zhan, J. Y.; Li, F.; Yu, F. S. A tandem strategy for enhancing electrochemical CO_2 reduction activity of single-atom Cu–S_1N_3 catalysts via integration with Cu nanoclusters. *Angew. Chem., Int. Ed.* **2021**, *60*, 24022–24027.

[35] Pei, J. J.; Shang, H. S.; Mao, J. J.; Chen, Z.; Sui, R.; Zhang, X. J.; Zhou, D. N.; Wang, Y.; Zhang, F.; Zhu, W. et al. A replacement strategy for regulating local environment of single-atom Co–S_xN_{4-x} catalysts to facilitate CO_2 electroreduction. *Nat. Commun.* **2024**, *15*, 416.

[36] Li, X. N.; Zeng, Y. Q.; Tung, C. W.; Lu, Y. R.; Baskaran, S.; Hung, S. F.; Wang, S. F.; Xu, C. Q.; Wang, J. H.; Chan, T. S. et al. Unveiling the *in-situ* generation of a monovalent Fe(I) site in the single-Fe-atom catalyst for electrochemical CO_2 reduction. *ACS Catal.* **2021**, *11*, 7292–7301.

[37] Li, K.; Zhang, S. B.; Zhang, X. L.; Liu, S.; Jiang, H. S.; Jiang, T. L.; Shen, C. Y.; Yu, Y.; Chen, W. Atomic tuning of single-atom Fe–N–C catalysts with phosphorus for robust electrochemical CO_2 reduction. *Nano Lett.* **2022**, *22*, 1557–1565.

[38] Wang, T. T.; Sang, X. H.; Zheng, W. Z.; Yang, B.; Yao, S. Y.; Lei, C. J.; Li, Z. J.; He, Q. G.; Lu, J. G.; Lei, L. C. et al. Gas diffusion strategy for inserting atomic iron sites into graphitized carbon supports for unusually high-efficient CO_2 electroreduction and high-performance Zn–CO_2 batteries. *Adv. Mater.* **2020**, *32*, 2002430.

[39] Jia, C.; Tan, X.; Zhao, Y.; Ren, W. H.; Li, Y. B.; Su, Z.; Smith, S. C.; Zhao, C. Sulfur-dopant-promoted electroreduction of CO_2 over coordinatively unsaturated Ni–N_2 moieties. *Angew. Chem., Int. Ed.* **2021**, *60*, 23342–23348.

[40] Maintz, S.; Deringer, V. L.; Tchougréeff, A. L.; Dronskowski, R. LOBSTER: A tool to extract chemical bonding from plane-wave based DFT. *J. Comput. Chem.* **2016**, *37*, 1030–1035.

[41] Dronskowski, R.; Bloechl, P. E. Crystal orbital Hamilton populations (COHP): Energy-resolved visualization of chemical bonding in solids based on density-functional calculations. *J. Phys. Chem.* **1993**, *97*, 8617–8624.